Investigating Active Site of Gold Nanoparticle $Au_{55}(PPh_3)_{12}Cl_6$ in Selective Oxidation

Yong Pei, Nan Shao, Yi Gao, and Xiao Cheng Zeng*

Department of Chemistry and Nebraska Center for Materials and Nanoscience, University of Nebraska-Lincoln, Lincoln, Nebraska, 68588

ABSTRACT We present an *ab initio* investigation of structural, electronic, catalytic, and selective properties of the ligand-covered gold nanoparticle $Au_{55}(PPh_3)_{12}Cl_6$ and associated model clusters. The catalytic activity of the $Au_{55}(PPh_3)_{12}Cl_6$ nanoparticle in the presence of O_2 stems from a combined effect of triphenylphosphine ligands and surface structure of the "magic-number" quasi-icosahedral Au_{55} core, which entails numerous ligand-encompassed triangle Au_6 faces as the active sites. Under the Eley-Rideal mechanism, the "triangle-socket" active site not only can accommodate one pre-adsorbed O_2 (which is subsequently activated to the superoxo species) with one styrene molecule at a time but also can provide spatial confinement which favors the formation of an oxametallacycle intermediate that leads to unique selectivity in styrene oxidation.

KEYWORDS: ligand-covered gold nanoparticles · catalytic properties and selectivity · active sites · quasi-icosahedral Au_{55} core · density-functional theory

Understanding the structure−activity−selectivity relationships of catalytic gold nanoparticles (AuNPs) is a challenging task. Gold nanoparticles in the size range of 1−3 nm exhibit extraordinary catalytic activity and selectivity in many industrially valuable reactions, for example, low-temperature oxidation of carbon monoxide, selective oxidation of olefin and alcohol, and water−gas shift reactions, *etc*.[1−16] Although catalytic activity of bare gold clusters (with or without support) is now reasonably understood,[17−28] characterization of the structure−activity−selectivity relationship for AuNPs in the size range of 1−3 nm remains elusive, largely due to the lack of precise atomic structure information of large-sized gold clusters. Previous studies have reported that catalytic activities of AuNPs can be greatly affected by a number of factors, for example, the size and shape of AuNPs, the ratio of low *versus* high coordinate sites, solvent effects, and interaction and charge transfer between AuNPs and metal oxide support.

The gas-phase gold clusters had been widely used as model systems to investigate chemical activity as a function of cluster size and structure. In particular, it has been found that the binding of an O_2 molecule on small-sized gold clusters ($N \leq 20$) is sensitive to the cluster size and charge states. The even-number Au_N^- anion clusters can strongly interact with O_2 molecule (with an exception of Au_{16}^-), while the odd-number Au_N^- clusters hardly interact with the O_2.[29,30] The neutral clusters Au_N, the positive charged Au_N^+ clusters, and the Au_N^- with large N were found inert toward the O_2 adsorption, with the exception of Au_{10}^{31} and Au_{10}^+.[32,33] Such a size depen-

dence has been explained on the basis of the electron affinity of Au_N^- clusters, that is, a low electron affinity requires higher free energy for the Au_N^-−O_2 binding.[29,30]

Gold clusters on metal oxide supports (*e.g.*, TiO_2 and MgO) show significantly enhanced activity and selectivity.[16,18−22] Chen *et al.* found that on a TiO_2 support Au bilayer nanostructures show a maximum reaction activity toward the CO, about 10 times higher than that on monolayer Au nanostructures, and 45 times faster than the most active Au/TiO_2 catalysts prepared from conventional methods.[8] Herzing *et al.* identified that bilayer Au clusters with a diameter of 0.5 nm and containing ∼10 atoms give rise to maximum activity toward the CO oxidation.[14] Landman and Heiz *et al.* showed that the charge transfer from the bottom F-center of MgO support to the Au_8 cluster plays a key role in promoting the chemical activity of Au_8 clusters.[19] Subsequent density functional theory (DFT) calculations confirmed the importance of the charge transfer between gold clusters and metal oxide to the enhancement of activity of Au clusters.[34−38] Sinha *et al.* reported that the silylated mesoporous titanosilicates
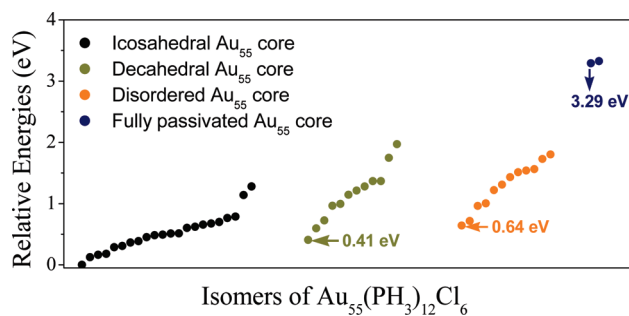
Figure 1. Relative energies of 48 isomer structures of $Au_{55}(PH_3)_{12}Cl_6$ (**Iso1** to **Iso48**, from low to high energy), optimized at the PBE/DNP level of theory.

support can greatly enhance the catalytic activity of gold catalysts for propylene epoxidation as well, even better than the TiO_2 support.[39]

Organic ligand-protected AuNPs are generally synthesized in solutions. In recent years, determination of the atomic structures of ligand-protected gold clusters have attracted considerable interest. Many previous studies have shown that ligand (such as mixed $-P(Ph)_3$ and $-Cl$, or the thiolate group $-SR$) protected gold clusters typically have a highly symmetric Au core.[40−53] The core size ranges from 0.5 to 1.3 nm. In general, ligand-protected Au clusters are considered ineffective for catalysis because the Au cores are mostly shielded by the ligands.[41−53] Recently, however, Tsunoyama et al. showed that the gold clusters stabilized by poly(N-vinyl-2-pyrrolidone) (PVP) and with a core size of 1.3 ± 0.3 nm can exhibit high catalytic activity for various aerobic oxidation reactions, such as oxidation of alcohol, homocoupling of arylboronic acids, generation of hydrogen peroxide from ammonium formate, and α-hydroxylation of benzylic ketones.[52] A mechanism for the high catalytic activity was attributed to the anionic Au core due to the electron donation effect of PVP molecules, which is akin to the electron-transfer mechanism between a gold cluster and a metal oxide support.[19,52] Another recent experimental study also demonstrated that the thiolate-protected Au_{25} nanocluster $[Au_{25}(SR)_{18}]$ can selectively catalyze the hydrogenation of α,β-unsaturated ketones and aldehydes under mild conditions.[53] The active sites for the C=O activation were likely at the eight open facets of the Au_{13} icosahedral core.

Also recently, Turner et al. reported that the ligand-covered 55-atom gold cluster $Au_{55}(PPh_3)_{12}Cl_6$ can exhibit relatively high activity and selectivity towards styrene oxidation,[10] as evident by the direct oxidation of styrene with O_2 to form benzaldehyde, styrene epoxide, and acetophenone.[10] Especially, the $Au_{55}(PPh_3)_{12}Cl_6$ cluster gives a conversion rate of 12.6% and selectivity of 13.1% toward styrene epoxide. Moreover, the $Au_{55}(PPh_3)_{12}Cl_6$ cluster provides higher selectivity toward benzaldehyde than to styrene epoxide and acetophenone.

In this article, we present a systematic ab initio study of low-lying structures of $Au_{55}(PPh_3)_{12}Cl_6$. Particular attention has been placed on seeking the active site on the Au_{55} core and a mechanism underlying the high selectivity of $Au_{55}(PPh_3)_{12}Cl_6$ in styrene oxidation. We found that the catalytic activity and selectivity of $Au_{55}(PPh_3)_{12}Cl_6$ can be attributed to a combination of several factors, including the quasi-icosahedral Au_{55} core structure and the ligand arrangement as well as the triphenylphosphine-surrounded triangle Au_6 face as the active site.

RESULTS AND DISCUSSIONS

Au_{55} Core Structure in $Au_{55}(PPh_3)_{12}Cl_6$. The structure of Au_{55} core in the $Au_{55}(PPh_3)_{12}Cl_6$ nanoparticle has been under debate since the first synthesis of the nanoparticles in 1981.[40] The cluster was hard to crystallize and therefore a single-crystal X-ray analysis was not possible. A cuboctahedral structure of Au_{55} core was first proposed by Schmid et al. based on Mössbauer, extended x-ray absorption fine structure (EXAFS), x-ray absorption near edge structure (XANES), and wide-angle x-ray scattering (WAXS) measurements as well as geometric consideration.[54,55] However, an icosahedral Au_{55} core structure was later suggested on the basis of the Debye-function analysis of X-ray diffraction (XRD) data.[56,57] To determine the most likely structure of the Au_{55} core, we performed geometric optimization of 49 different structures of $Au_{55}(PR_3)_{12}Cl_6$ (labeled as **Iso-1** to **Iso-49**), but the original phenyl groups were replaced by $-H$ (e.g., R = $-H$) to reduce computational cost. Three groups of Au_{55} core structures were considered: (a) three high-symmetry Au_{55}-core structures composed of icosahedral (I_h), cubotahedral (O_h), and decahedral (D_{5h}) structures; (b) five low-symmetry disordered Au_{55} structures, derived from a global-minimum search using the basin-hopping method,[58,59] composed of the top five lowest-lying isomers among 200 low-energy Au_{55} isomers; the lowest-lying Au_{55} isomer is 0.47, 1.40, and 1.97 eV lower in energy than the I_h, D_{5h}, and O_h Au_{55} cluster, respectively, based on the PBE/DNP level of theory (see Computational Methods). Our result is consistent with a recent joint experimental and theoretical study in that the lowest-energy isomer of anion Au_{55}^- exhibits a disordered structure;[60] (c) two Au_{55} structures which are composed of a Au_{37} nucleus and a Au_{18} shell, where each Au atom in the Au_{18} shell is directly bonded with one of 18 ligands (e.g., $[Au_{37-nucleus}][Au_{18}(PH_3)_{12}Cl_6]$).

Figure 1 illustrates relative energies of totally 48 isomers of $Au_{55}(PH_3)_{12}Cl_6$. The O_h-Au_{55} core-based structure (**Iso-49**) was not included since the O_h-Au_{55} core was converted to a quasi-I_h-Au_{55} core after geometric optimization. In general, the I_h-Au_{55} core-based (**Iso-1** to **Iso-22**) and D_{5h}-Au_{55} core-based (**Iso-23** to **Iso-34**) isomers possess relatively lower energies. The lowest-energy isomer (**Iso-1**) has a quasi-I_h-Au_{55} core, and it is 0.41 eV lower in energy than the lowest-energy D_{5h}-Au_{55}
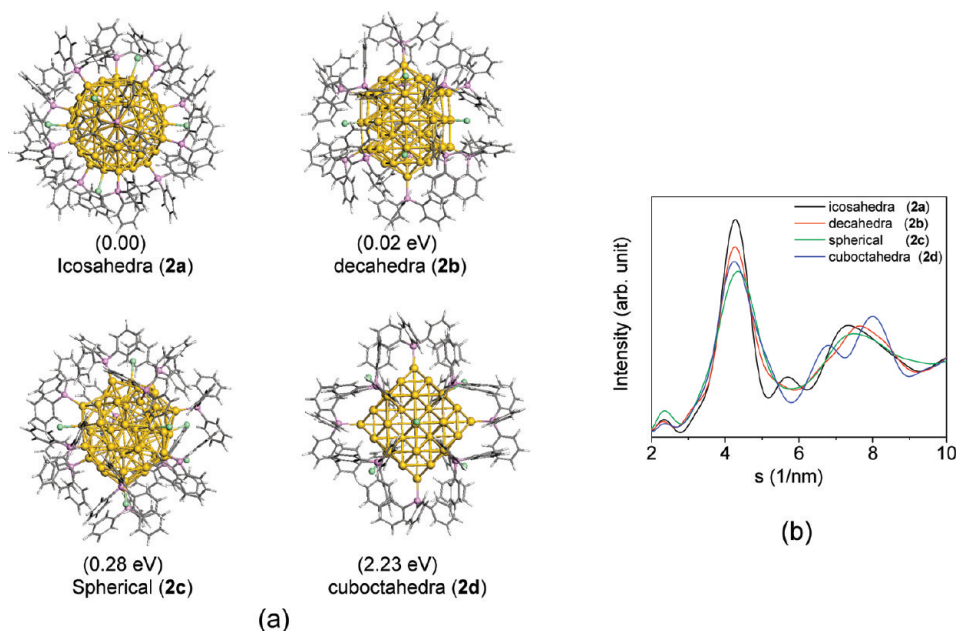
Figure 2. (a) Optimized structures and relative energies of icosahedral (**2a**), decahedral (**2b**), disordered (**2c**), and cubocta-hedral (**2d**) Au_{55} core-containing $Au_{55}(PPh_3)_{12}Cl_6$ isomers. (b) A comparison of simulated XRD patterns of the four isomer structures. Color code: Au (gold), C (green), P (purple), C (grey), and H (white).

core-based isomer (**Iso-23**) and 0.64 eV lower than the disordered Au_{55} core-based isomer (**Iso-35**). **Iso-47** and **Iso-48** have fully passivated Au_{55} cores, and they are much higher in energy (> 3 eV) than **Iso-1**. The energy ordering among the 48 $Au_{55}(PH_3)_{12}Cl_6$ isomers indicate that the —PH_3 ligands can stabilize both the quasi-I_h-Au_{55} and quasi-D_{5h}-Au_{55} cores. Similar behavior has been observed in small-sized ligand-protected gold clusters, for instance, the quasi-I_h-Au_{13} core in $[Au_{13}(PMe_2Ph)_{10}Cl_2]^{3+}$ cluster and the hexagonal anti-prismatic D_3-Au_{39} core in $[Au_{39}(Ph_3P)_{14}Cl_6]^{2+}$ cluster.[61,62]

Note that the simplified model structures of $Au_{55}(PH_3)_{12}Cl_6$ shown above provide only approximate structures for the $Au_{55}(PPh_3)_{12}Cl_6$ nanoparticles. In fact, the replacement of the phenyl group by —H in the sim-plified model $Au_{55}(PH_3)_{12}Cl_6$ can lead to a strong hydrogen-bonding interaction between the —PH_3 and —Cl groups and can also underestimate non-bonding repulsion among the —PPh_3 ligands in $Au_{55}(PPh_3)_{12}Cl_6$. We performed additional geometric optimization of three triphenylphosphine-covered $Au_{55}(PPh_3)_{12}Cl_6$ iso-mers which possess a quasi-I_h-, a quasi-D_{5h}-, and a disor-dered Au_{55} core, respectively. The three more realistic structures are labeled as **2a**, **2b**, and **2c**, respectively. The initial Au_{55} core geometries and ligand arrange-ments of **2a**, **2b**, and **2c** were identical to those of **Iso-15**, **Iso-23**, and **Iso-35**, except the —PH_3 groups were replaced by —PPh_3 groups. In **2a** and **2b**, the 12 —PPh_3 groups occupy 12 vertices of a Au_{55} core to minimize steric interactions. We also considered an O_h-Au_{55} core-based isomer of $Au_{55}(PPh_3)_{12}Cl_6$ (namely, **2d**), built with six —Cl ligands attached to the center Au atom on the six quadrangle faces, which is a homologue to the struc-ture originally proposed by Schimd *et al.*[54,55] Figure 2a

displays optimized structures and relative energies of **2a**—**d**. The structures **2a** and **2b** containing a quasi-I_h and quasi-D_{5h}-Au_{55} core, respectively, are nearly isoen-ergetic (with an energy difference less than 0.02 eV), while **2c** and **2d** are 0.28 and 2.23 eV higher in energy than **2a**, respectively. This energy ordering is consistent with that obtained from the simplified model $Au_{55}(PH_3)_{12}Cl_6$ (Figure 1). Note also that the arrange-ment of —Cl groups on the quasi-I_h-Au_{55} (**2a**) or quasi-D_{5h}-Au_{55} (**2b**) core is somewhat arbitrary due to small energy differences (<0.2 eV; see Figure 1) among differ-ent ligand arrangements.

Our prediction of the quasi-I_h-Au_{55} core for $Au_{55}(PPh_3)_{12}Cl_6$ nanoparticle is consistent with earlier XRD studies.[56,57] We note that the quasi-I_h-Au_{55} core structure was also concluded in a recent theoretical study of $Au_{55}(PH_3)_{12}Cl_6$.[63] In Figure 2b, we display simu-lated XRD patterns for **2a**—**d** based on the Debye-function analysis (see Computational Methods). The first major peak (at ~4.2 nm^{-1}) of simulated XRD pat-terns of **2a**—**c** is in good agreement with that of the ex-perimental one,[56] but that of **2d** is not because of the presence of two peaks in the 6—9 nm^{-1} region. The simulated XRD spectrum of **2a** exhibits another weaker peak at 5.7 nm^{-1} while a weak peak at ~4.9 nm^{-1} was also observed in the experiment (Figure 6 in ref 55). De-spite the difference in the location of the weak peak, it seems that the structure of quasi-I_h-Au_{55} core-based iso-mer **2a** is closer to the isomer detected in the XRD ex-periment (ref 55) than that of isomer **2b** and **2c**, in light of this weak signature peak.

Structure—Activity Relationship of $Au_{55}(PPh_3)_{12}Cl_6$. In the quasi-I_h-Au_{55} core-based $Au_{55}(PPh_3)_{12}Cl_6$ (**2a**), the 12 —PPh_3 ligands occupy 12 vertices of the quasi-I_h-Au_{55}
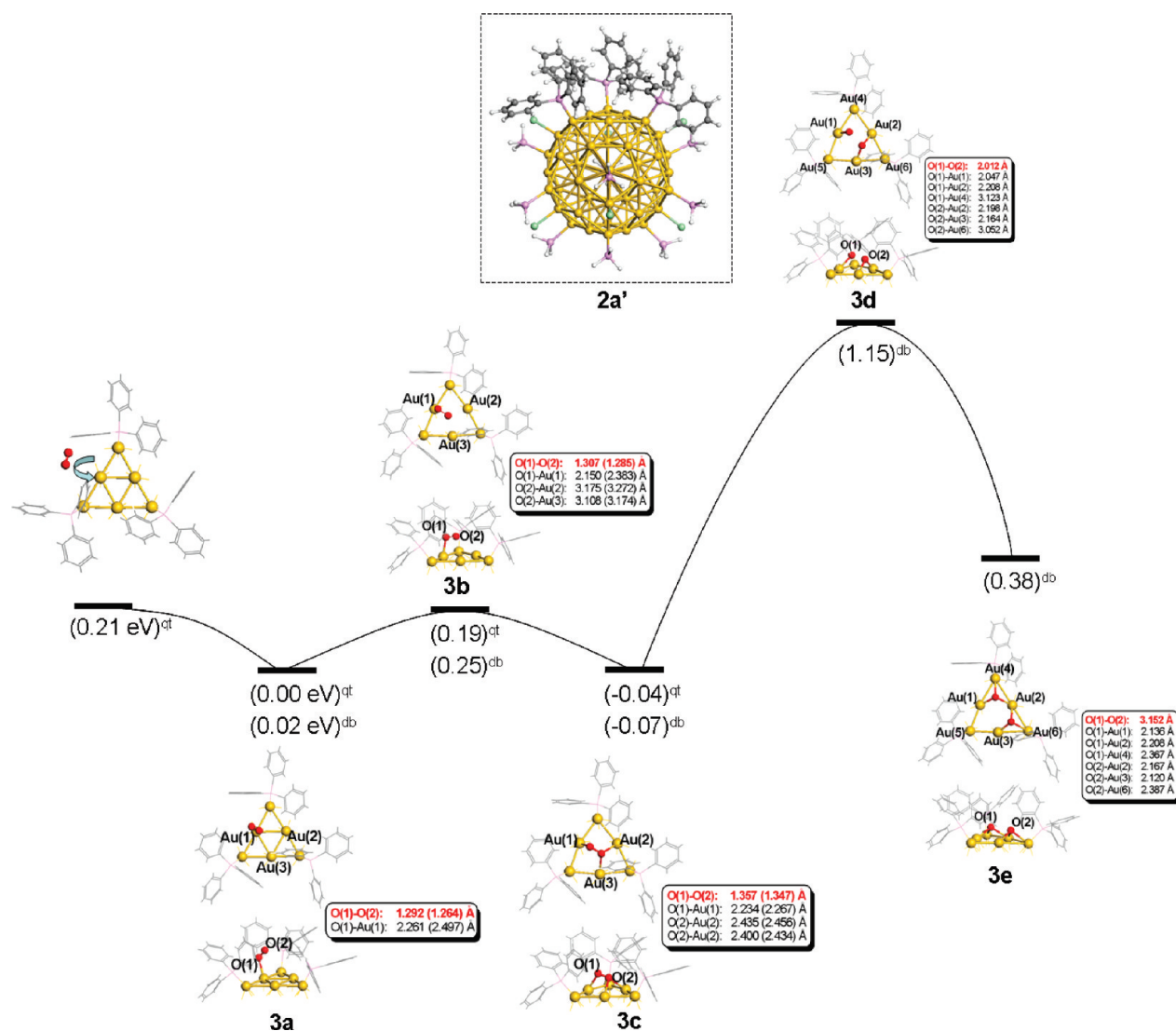
Figure 3. The O_2 dissociation pathway on the triangle Au_6 active site encompassed by —PPh_3 ligands, which is calculated on the basis of a model system **2a**′. The energy is in units of eV. The superscripts qt and db represent the quartet and doublet spin states, respectively. For states **3a-3c**, both top and side views are shown. The bond lengths shown in parentheses correspond to the quartet spin state of **3a-3c**.

core. Hence, only edge sites and triangle Au_6 faces can be potential active sites for O_2 adsorption and activation. To compute the O_2 dissociation pathway, we used a simplified model **2a**′ which is derived from **2a** by keeping only three —PPh_3 groups for encompassing a triangle Au_6 face while all other —PPh_3 groups are replaced by —PH_3 groups (Figure 3). Both doublet and quartet spin states were examined when computing the O_2 dissociation pathway.

It is worth noting that, on the basis of the lowest-lying Au_{55} cluster obtained from the basin-hopping search, it appears the bare Au_{55} is chemically quite inert toward O_2 activation. An O_2 dissociation route is computed and shown in Supporting Information Figure S1. We found that a fairly high energy barrier (1.95 eV) is required for the O_2 dissociation when the O_2 is adsorbed at a triangle-like surface site. Such a high energy barrier indicates that the bare disordered Au_{55} cluster, based on our model, is unlikely to catalyze O_2 dissociation.

As shown in Figure 3, when O_2 is adsorbed on the triangle Au_6 face, the activation of O_2 takes two steps: the formation of a superoxo-like species (**3a** to **3c**) and the dissociation of superoxo species into two O atoms (**3c** to **3d**). Initially, an O_2 molecule is adsorbed on an edge site (**3a**) with an adsorption energy of −0.21 eV, where the whole system is at quartet spin ground state. The O—O bond length is 1.264 Å (about 0.06 Å longer than the gas phase O—O bond length). The net spin population on two O atoms is 0.71 and 0.80, respectively (*cf.* Supporting Information Table S1), indicating that O_2 is scarcely activated. The barrier for O_2 activation from **3a** to **3c** is 0.19 eV and the process is slightly exothermic (−0.07 eV). Note that for **3c** the doublet spin state gives rise to a lower energy than the quartet spin state. At the intermediate state **3c**, the O—O bond is elongated to ~1.36 Å, and the spin population on the two O atoms decreases to 0.13 (*cf.* Table S1). Charge analysis shows that both O atoms are *negatively charged* (*cf.*
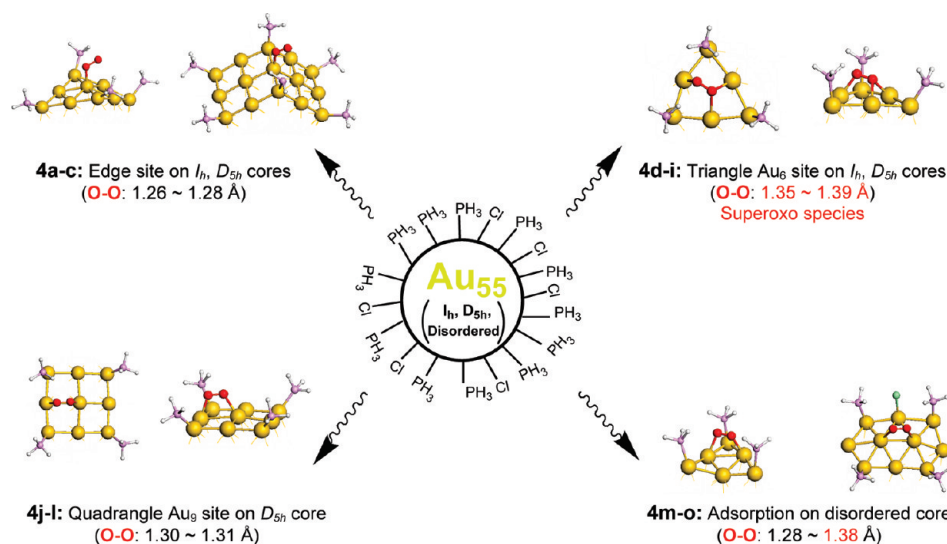
Figure 4. Summarization of O_2 adsorption and activation on four types of surface site on the $Au_{55}(PPh_3)_{12}Cl_6$ nanoparticle with different Au_{55} core structures: **4a,b,d–g** are based on isomers with quasi-I_h-Au_{55} and quasi-D_{5h}-Au_{55} core isomers; **4h–l** are based on isomers with decahedral Au_{55} core; **4m,n** present adsorption sites on isomers with the disordered Au_{55} core. Detailed geometries of various adsorption modes (**4a–o**) and the spin/charge distributions of O and Au atoms are given in Figure 5 and Supporting Information Table S1, respectively.

Table S1), confirming the formation of a superoxo-like species. Next, the barrier from the intermediate state **3c** to O_2 dissociation state **3e** is 1.22 eV, about 0.6 eV lower than the barrier to O_2 dissociation on the Au(111) surface (~1.80 eV) but comparable to that on the step of Au(211).[64] Note also that the experiment[10] was carried out at ~100 °C, which can further promote O_2 dissociation. Although the O_2 dissociation is endothermic, a relatively high association barrier (~0.77 eV from **3e** to **3d**) may hinder the reverse reaction. At the dissociation state **3e**, the two O atoms are separated by 3.15 Å with each O adsorbed on a threefold fcc hollow site.

A number of sites for O_2 adsorption on the homologue $Au_{55}(PH_3)_{12}Cl_6$ with different Au_{55} core structures (from the isomer database shown in Figure 1) were examined. Figures 4 and 5 list 15 representative O_2 adsorption sites, including edge sites (**4a–c**) and triangle faces (**4d–i,m**), as well as quadrangle faces (**4j–l**) on the D_{5h}-Au_{55} core and a few irregular sites (**4n,o**) on the disordered Au_{55} core. Here, **4g** has the same ligand arrangement as **3c**. Adsorption energies, charge, and spin densities on O atoms for **4a–o** are given in Supporting Information Table S1. By comparing the O–O bond length in **4g** and **3c**, it can be seen that the replacement of phenyl group by —H incurs little change on the O–O bond length in the superoxo species, validating the use of simplified model $Au_{55}(PH_3)_{12}Cl_6$ for testing O_2 activation. As shown in Figures 4 and 5, the O–O bond length is significantly elongated when O_2 is located near the triangle Au_6 face (**4d–i,m**), regardless of the Au_{55} core structure, arrangement of ligands, and spatial orientation of O_2.

Upon O_2 adsorption, electron transfer takes place from Au to O due to stronger electronic affinity of the

O atom. On the triangle Au_6 face (**4d–i,m**), the electron transfer (δ_{Au}) is much more than that on other type sites. The three inner Au atoms (Au(1), Au(2), and Au(3); see Figure 5) of the triangle Au_6 face are mainly involved in the charge transfer (cf. Supporting Information Table S1). All Au–Au bonds on the triangle active sites are significantly stretched upon O_2 adsorption (cf. **4d–i** in Figure 5). Spin-density analysis shows that the net spin on the two O atoms is fairly small in **4d–i,m** (<0.30 for each O atom), consistent with strong activation of O_2. On the quadrangle face of **4j–l**, O_2 is moderately activated, as evident from modest elongation of O–O bond length (~1.31 Å) and spin density on O atoms (cf. Figure 5 and Supporting Information Table S1). On an edge site (**4a–c**) or an irregular face (**4n,o**), O_2 is only weakly activated. The charge on each O atom is less than 0.01 e and the spin density is close to that of gas-phase O_2 in **4a–c,n,o**. In addition, we examined numerous adsorption sites on 11 isomers containing the disordered-Au_{55} core (**Iso-35** to **Iso-46** in Figure 1). No evidence of strong O_2 activation was found. We therefore conclude that the —PPh_3 encompassed triangle Au_6 face is the primary *active site* on $Au_{55}(PPh_3)_{12}Cl_6$. The quasi-I_h-Au_{55} core possesses 20 triangle Au_6 faces, offering the largest number of active sites for O_2 activation; the D_{5h}-Au_{55} core possesses 10 triangle Au_6 faces, while the disordered-Au_{55} core has an irregular surface with fewer active sites.

The underlying mechanism for the activity of the —PPh_3-encompassed triangle Au_6 face is due to several factors. First, at the 12 vertices of the quasi-I_h-Au_{55} core, the —PPh_3 ligand strongly binds with the undercoordinated vertex Au site. A back donation of electrons from P to the vertex Au renders all unpassivated edge
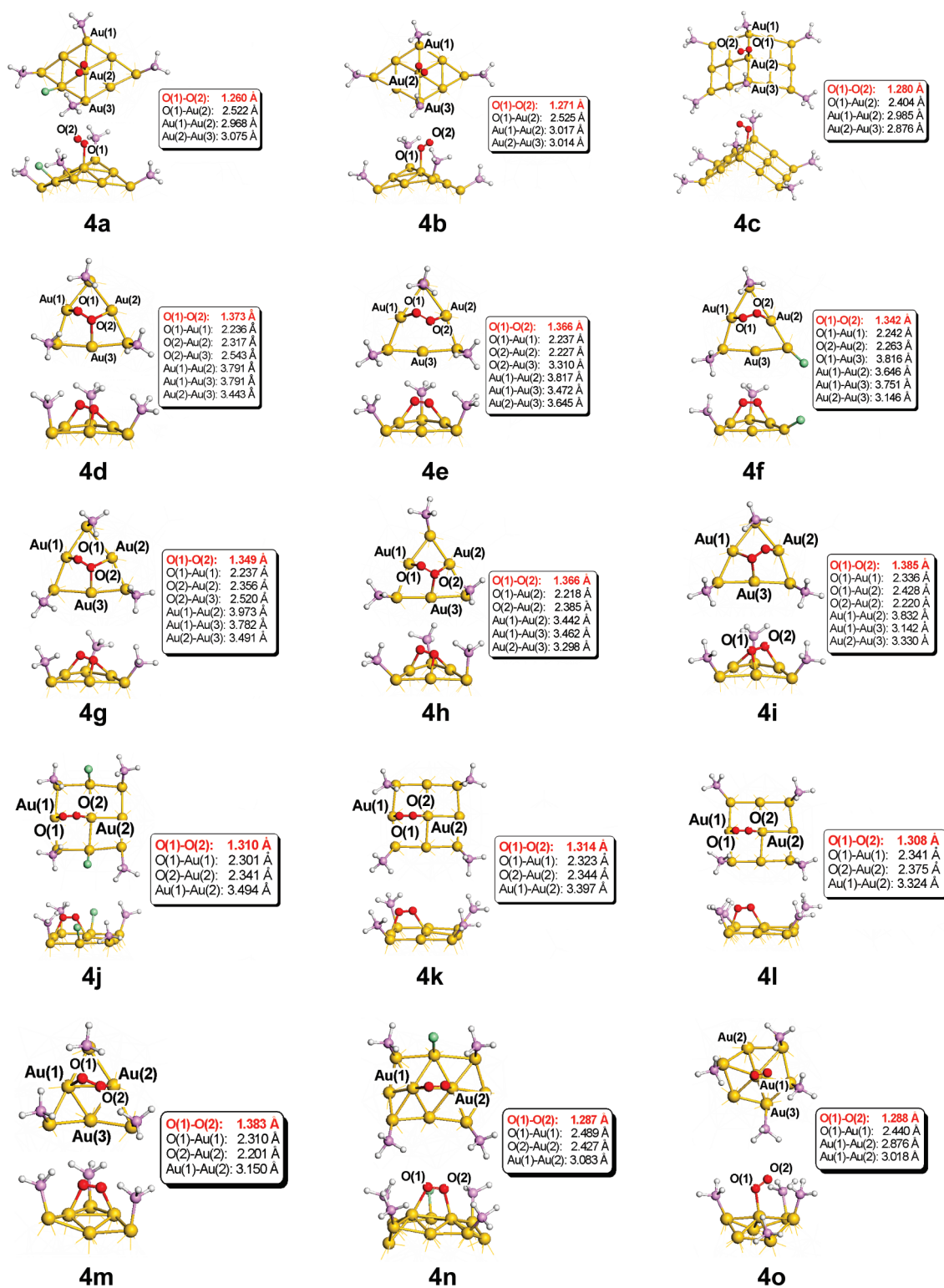
Figure 5. Local geometries of O_2 adsorbed on various sites with different Au_{55} core structures: **4a,b,d–g** are based on isomers with quasi-I_h-Au_{55} and quasi-D_{5h}-Au_{55} cores; **4h–l** are based on isomers with decahedral Au_{55} core; **4m,n** represent adsorption sites on isomers with the disordered Au_{55} core.

Au atoms *negatively charged*. The negatively charged Au atoms at the edge of $Au_{55}(PPh_3)_{12}Cl_6$ lead to strong O_2 activation. A similar mechanism was found for the supported Au_8 cluster on the MgO surface,[19] where Au_8 is negatively charged due to the F-center on the MgO surface. In Figure 6a–c, we plot the partial density of state (PDOS) of an edge Au atom in the triangle Au_6 face for both bare I_h-Au_{55} and ligand-covered quasi-I_h-Au_{55} (**2a′**) clusters, and the DOS of the O_2 molecule. The Fermi energy of the Au atom is shifted to a higher en-
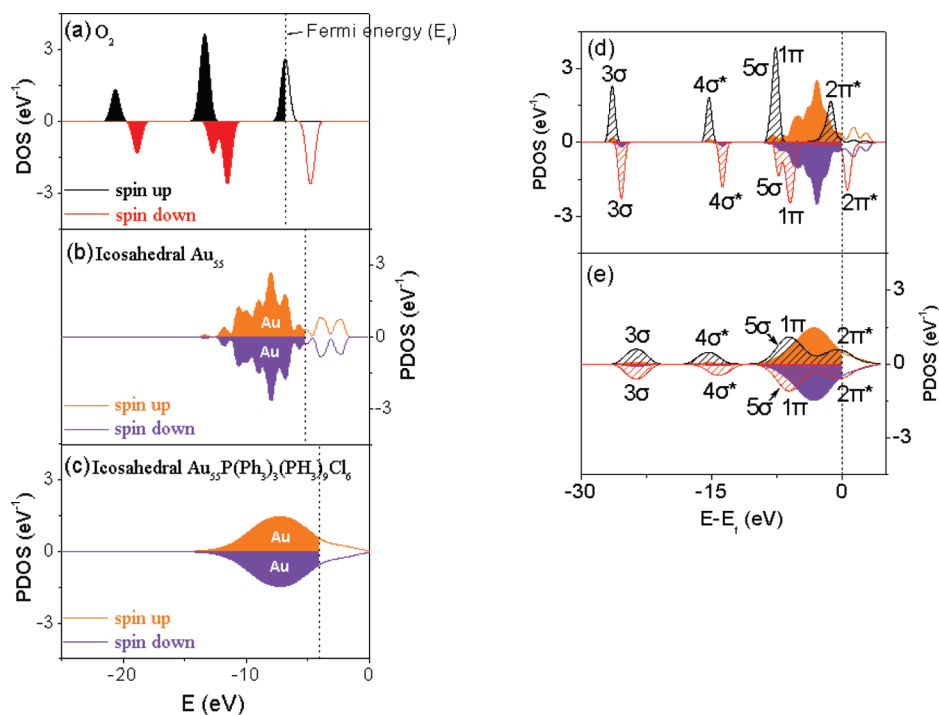
**Figure 6.** (a) DOS of O_2 molecule; (b) PDOS of an edge Au atom on the triangle Au_6 face for a bare I_h-Au_{55} cluster and that for a (c) ligand-covered quasi-I_h-Au_{55} cluster (**2a**′); (d) PDOS of an adsorbed O_2 and PDOS of an edge Au atom on the triangle Au_6 face for the bare I_h-Au_{55} cluster; (e) PDOS of an adsorbed O_2 and PDOS of an edge Au atom on the triangle Au_6 face for ligand-covered qausi-I_h-Au_{55} cluster (**3c**, *cf.* Figure 3). Orange and violet areas represent PDOS of the Au atom. The black and red lines represent DOS of the O_2 molecule.

ergy due to the presence of ligands (Figure 6c), resulting in more overlap between the highest occupied molecular orbital (HOMO) of the Au atom and the lowest unoccupied molecular orbital (LUMO) (down-spin $2\pi^*$) of O_2. Moreover, the spatial orientation of the HOMO of **2a**′ (Supporting Information Figure S2) matches nicely with the $2\pi^*$ (LUMO) of O_2 at the triphenylphosphine-encompassed triangle Au_6 face, facilitating orbital interaction and electron transfer. Figures 6 panels d and e display the PDOS of O_2 adsorbed on the bare I_h-Au_{55} cluster and the ligand-covered Au_{55} (**2a**′), respectively. A strong resonance between the $2\pi^*$ orbital of O_2 and the 5d and 6s bands of the edge Au atom occurs on **2a**′. The spin-down $2\pi^*$ orbital is partially occupied due to the charge transfer from Au to O. In contrast, less orbital resonance is seen for O_2 adsorbed on the bare I_h-Au_{55} cluster (Figure 6d) as the spin-down $2\pi^*$ orbital of O_2 remains unoccupied. These observations indicate that the ligands in $Au_{55}(PPh_3)_{12}Cl_6$ not only stabilize the Au_{55} core, but also significantly affect the electronic structure of the inner Au core. We note that such a promotion effect of O_2 activation by linking the electron-donation ligands on gold clusters was also proposed independently in recent experimental[52] and theoretical[65] studies.

Selectivity in Styrene Oxidation. Another intriguing property of $Au_{55}(PPh_3)_{12}Cl_6$ is its catalytic selectivity in styrene oxidation. Turner *et al.* reported that, for styrene oxidation, $Au_{55}(PPh_3)_{12}Cl_6$ gives rise to a much higher yield of benzaldehyde than styrene epoxide and acetophenone.[10] This selectivity can be attributed to the special local geometry of the active site (—PPh₃-encompassed triangle Au_6 face), named as a "triangle socket" here in light of the spatial confinement by surrounding ligands. In Scheme 1, four probable reaction pathways under Eley-Rideal mechanism[19,20,26,31,66−68] are shown, as well as the corresponding energy diagrams, for the case when a styrene molecule, along with pre-adsorbed two O atoms, is trapped in the "triangle socket". Figure 7 displays corresponding molecular snapshots and diagrams of the intermediate and transition states associated with the four reaction pathways.

On a bare gold cluster or surface, a known step for styrene oxidation is the initial formation of the oxametallacycle (OMME) intermediate through an electrophilic attack of C═C double bond to a positively charged gold moiety.[69−71] With an oxygen atom adsorbed on I_h-$Au_{55}(PPh_3)_{12}Cl_6$ (**3e**), the Au(2) site (*cf.* Figure 3) possesses a significant amount of positive charge due to its interaction with two O atoms. Thus, the reaction pathway for styrene oxidation starts most likely from an initial attack of the Au(2) site by the C═C double bond. Scheme 1a presents four most probable reaction pathways for the styrene oxidation. The corresponding energy diagram (scheme 1b) shows that trapping a styrene molecule in the triangle active site is exothermic (-0.95 eV), and the energy barrier for the subsequent formation of the OMME intermediate (**6**→**6b**) is 0.90 eV, with the energy release
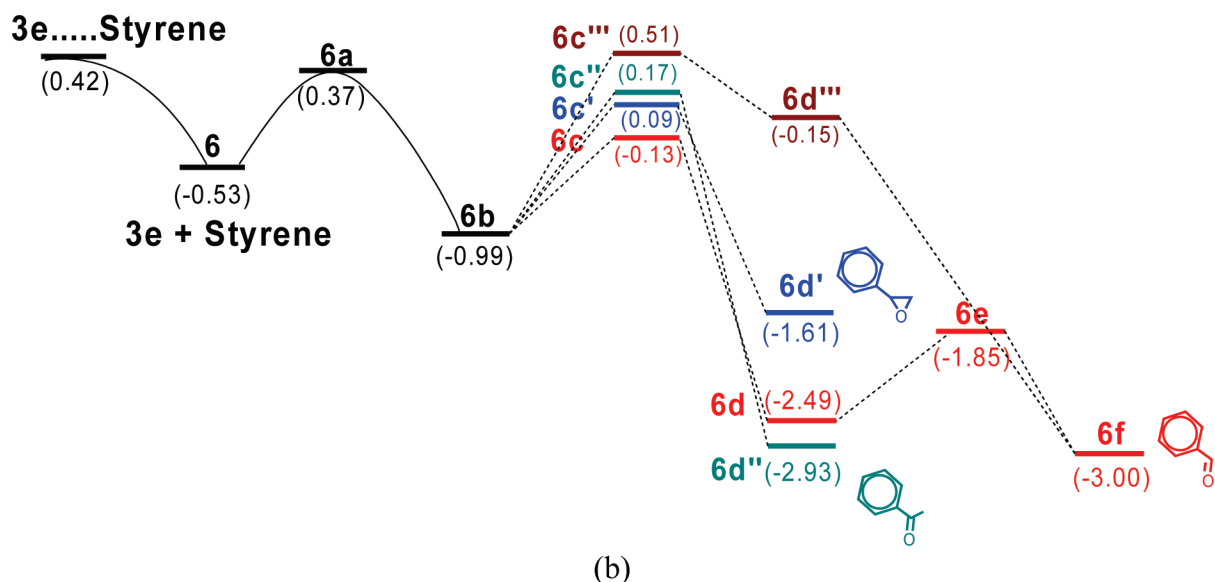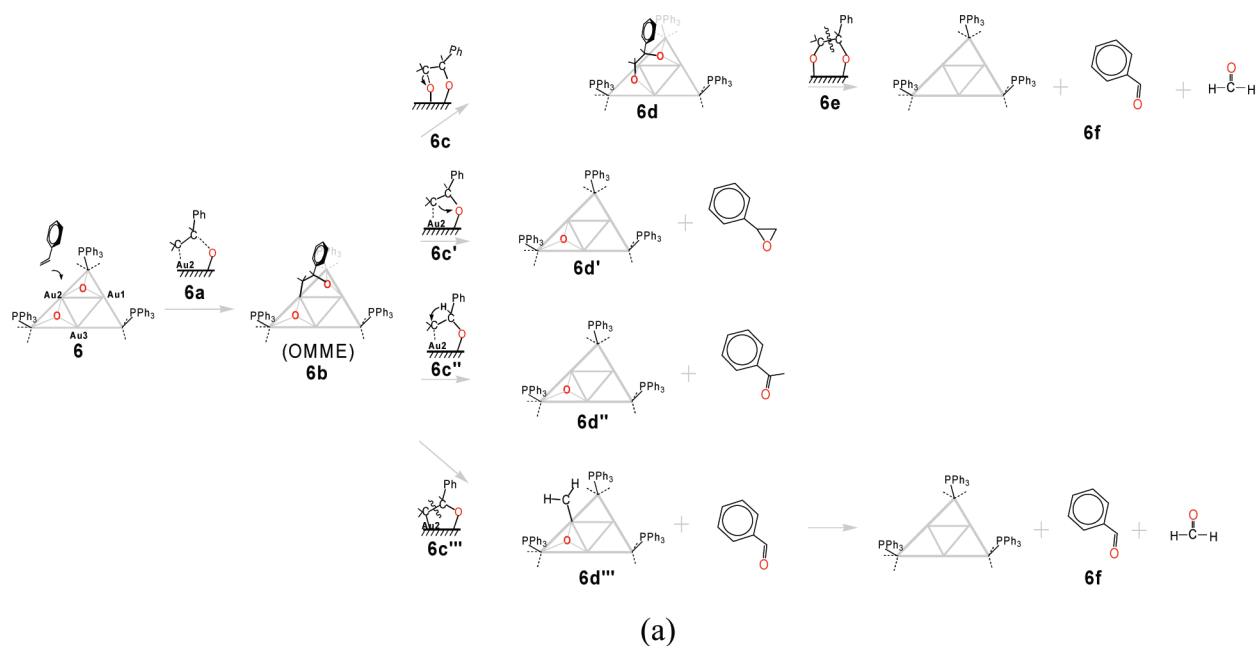
Scheme 1. (a) Four styrene oxidation pathways at the ligand-encompassed triangle Au₆ active site. (b) Energy diagrams for the oxidation reactions shown in panel a. Snapshots of key reaction intermediates and transition states are available in [Figure 7]. The energy is in units of eV. The energy curve in panel b is continued by the O₂ dissociation pathway in [Figure].

of 1.36 eV. Starting from the OMME intermediate (**6b**), four pathways (through transition states **6c**, **6c′**, **6c′′**, **6c′′′**, respectively) are possible toward the formation of three different products as illustrated in Scheme 1a. As shown in Scheme 1a,b, the most favorable pathway (**6b**→**6c**→**6d**→**6e**→**6f**) entails a key step for the formation of a second OMME intermediate (**6d**) which involves two C−O bonds with both oxygens bonded to gold atoms underneath. The activation energy to the formation of the second OMME intermediate (**6b**→**6d**) is 0.22 eV lower than that in the epoxide process (**6b**→**6d′**), and 0.30 eV lower than the intramolecular hydrogen transfer reaction (**6b**→**6d′′**). Finally, the benzaldehyde (and form-

aldehyde) can readily form through the path (**6d**→**6f**) with a low-energy barrier (0.64 eV), which involves the breaking of the C−C bond. This path is responsible for a very high yield of benzaldehyde. In contrast, the energy barrier (1.5 eV) through the path **6b**→**6d′′′** is much higher than that (0.86 eV) through **6b**→**6d**, suggesting that the formation of the second OMME intermediate containing two C−O bonds is a critical step to the high yield of benzaldehyde.

CONCLUSIONS

We show that Au₅₅(PPh₃)₁₂Cl₆ nanoparticles likely possess a quasi-I_h-Au₅₅ core. The ligands not only can ef-
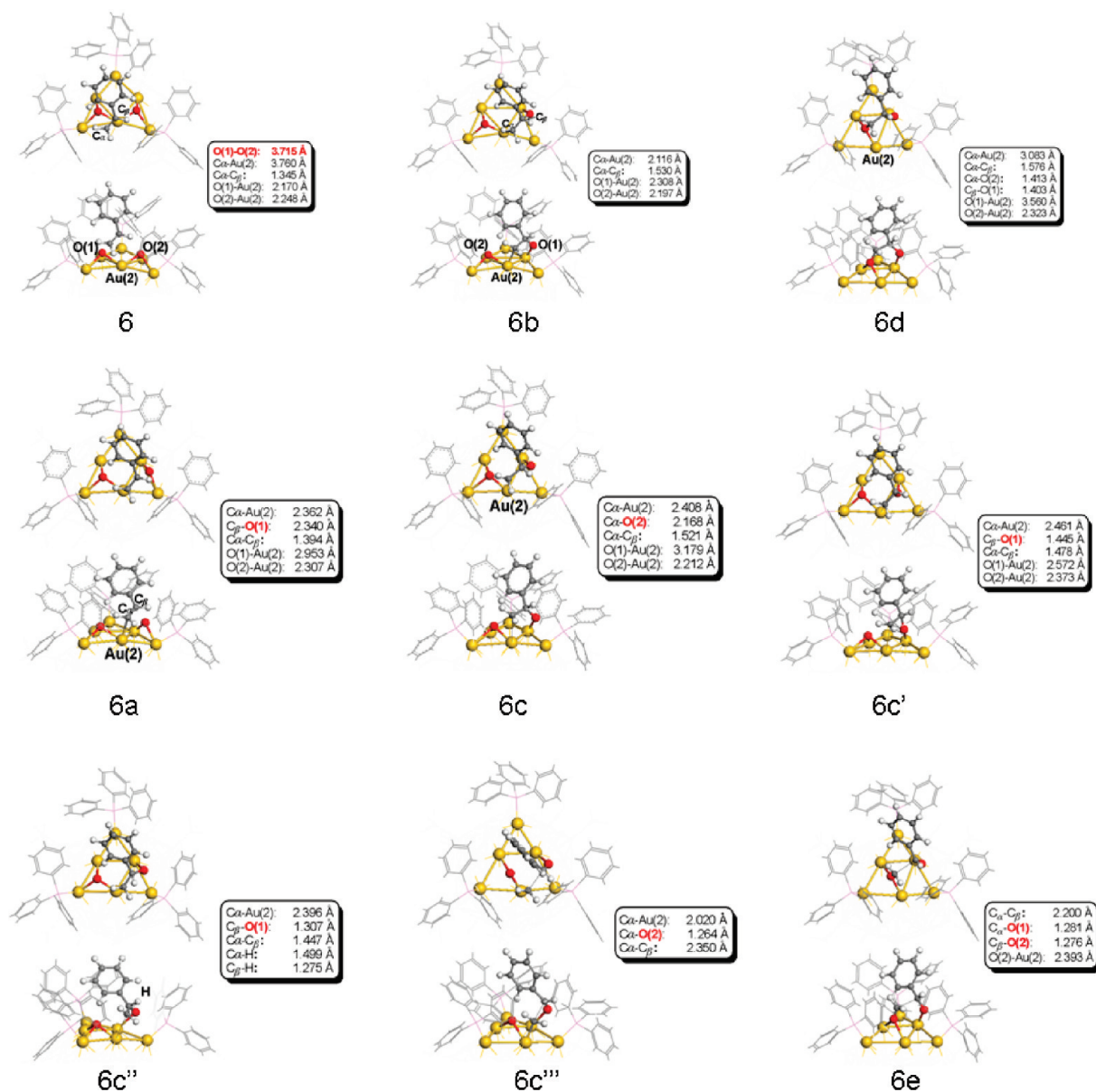
Figure 7. Snapshots of key reaction intermediates and transition states in the styrene oxidation pathway shown in Scheme 1.

fectively stabilize the quasi-I_h-Au_{55} core structure but also can significantly affect the electronic structure of the inner gold cluster. The catalytic activity of the $Au_{55}(PPh_3)_{12}Cl_6$ nanoparticle in the presence of O_2 stems from a *combined* effect of triphenylphosphine ligands and surface structure of the "magic-number" quasi-I_h-Au_{55} core, which entails numerous ligand-encompassed triangle Au_6 faces as active sites. The electron back-donation from the —P(PPh_3)_3 groups makes the Au_{55} core negatively charged. The negative charged and low-coordinated Au atoms in the active site facilitate O_2 activation. Furthermore, the spatial confinement by ligands gives rise to a new form of OMME intermediate containing two C—O bonds, leading to a high yield of benzaldehyde in the styrene oxidation. Identification of the ligand—encompassed gold active site will facilitate improved molecular design of a ligand-covered

nanogold catalyst. Finally, we note that Turner *et al.* have also reported that the removal of ligands by heat treatment can significantly increase the activity and selectivity of Au nanoparticles around the size of 1.4 nm or smaller.[10] Recent DFT calculations showed that catalytic activity of a bare Au_{55} nanocluster can be strongly dependent on the structure of the cluster.[28] Hence, a complete understanding of the unique catalytic activity and selectivity of bare Au nanoclusters around 1.4 nm (after heat treatment) must await experimental determination of atomic structure of these gold clusters. In future, we will investigate structure-activity-selectivity relationship of the ligand-covered cluster under the Langmuir-Hinshelwood mechanism.[19,20,26,31,66,67] This mechanism requires co-adsorption of both O_2 and styrene molecules at the active site. Research in this direction is under way.

COMPUTATIONAL METHODS

Density functional theory (DFT) calculations were carried out using the DMol3 4.3 package.[69] Geometric optimization of $Au_{55}(PPh_3)_{12}Cl_6$ and $Au_{55}(PH_3)_{12}Cl_6$ nanoparticles were performed by using the generalized gradient approximation in the form of the Perdew−Burke−Ernzerhof (PBE) functional,[73] as used in many previous theoretical studies of gold cluster catalysis.[74−76] The d-polarization-included basis set (DNP) with the effective core potential (ECP) including partial consideration of scalar relativity for the Au element was chosen.[77,78] All-electron calculations were otherwise applied for H, C, Cl, and P elements.

The self-consistent-field calculation has convergence criteria of 10^{-5} Hartree. The tolerances of energy, maximum force, and maximum displacement for the geometry optimization were set to be 1.0×10^{-5} au, 0.003 au, and 0.005 au, respectively. Optimization convergence thresholds for the root-mean-square forces on the atoms were set to be 0.002 au in transition-state search. The combined linear synchronous transit (LST) and quadratic synchronous transit (QST) methods were adopted to locate the transition state.

Theoretical XRD patterns are calculated based on the Debye formula:

$$I(s) = \sum_i \sum_{j \neq i} \frac{\cos \theta}{(1 + \alpha \cos 2\theta)} \exp\left(-\frac{Bs^2}{2}\right) f_i f_j \frac{\sin(2\pi d_{ij})}{2\pi d_{ij}}$$

where s is the diffraction vector length, satisfying $s = 2 \sin \theta/\lambda$. The wavelength λ and α parameter are 0.1051967 nm and 1.01, respectively (determined from the experimental set-up); B is 0.03 nm^2, a damping factor reflecting thermal vibration; d_{ij} is the distance between atoms i and j. The corresponding atomic numbers are used for the scattering factors f_i.

Supporting Information Available: Adsorption energies, Hirshfield charges, Mulliken spin density of O_2 adsorption on various active sites, and an energy profile for the O_2 dissociation on a reaction site of Au_{55}. This material is available free of charge *via* the Internet at http://pubs.acs.org.

REFERENCES AND NOTES

1. Haruta, M. Size- and Support-Dependency in the Catalysis of Gold. *Catal. Today* **1997**, *36*, 153–166.
2. Min, B. K.; Friend, C. M. Heterogeneous Gold-Based Catalytic for Green Chemistry: Low-Temperature CO Oxidation and Propylene Oxidation. *Chem. Rev.* **1998**, *107*, 2709–2724.
3. Chen, M.; Goodman, D. W. Catalytically Activate Gold: From Nanoparticles to Ultrathin Films. *Acc. Chem. Res.* **2006**, *39*, 739–746.
4. Hashmi, A. S. K.; Hutchings, G. J. Gold Catalysis. *Angew. Chem., Int. Ed.* **2006**, *45*, 7896–7936.
5. Sinha, A. K.; Seelan, S.; Tsubota, S.; Haruta, M. Catalysis by Gold Nanoparticles: Epoxidation of Propylene. *Top. Catal.* **2004**, *29*, 95–102.
6. Bond, G. C.; Thompson, D. T. Catalysis by Au. *Catal. Rev. Sci. Eng.* **1999**, *41*, 319–388.
7. Haruta, M.; Yamada, N.; Kobayashi, T.; Iijima, S. Au Catalysts Prepared by Coprecipitation for Low-Temperature Oxidation of Hydrogen and of Carbon-Monoxide. *J. Catal.* **1989**, *115*, 301–309.
8. Chen, M. S.; Goodman, D. W. The Structure of Catalytically Active Gold on Titania. *Science* **2004**, *306*, 252–255.
9. Hughes, M. D.; Xu, Y.; Jenkins, P.; McMorn, P.; Landon, P.; Enache, D. I.; Carley, A. F.; Attard, G. A.; Hutchings, G. J.; King, F.; *et al.* Tunable Gold Catalysts for Selective Hydrocarbon Oxidation under Mild Conditions. *Nature* **2005**, *437*, 1132–1135.
10. Turner, M.; Golvoko, V. B.; Vaughan, O. P. H.; Abdulkin, P.; Berenguer-Murcia, A.; Tikhov, M. S.; Johnson, B. F. G.; Lambert, R. M. Selective Oxidation with Dioxygen by Gold Nanoparticle Catalysts Derived from 55-Atom Clusters. *Nature* **2008**, *454*, 981–983.
11. Fu, Q.; Saltsburg, H.; Flytzani-Stephanopoulos, M. Active Nonmetallic Au and Pt Species on Ceria-Based Water−Gas Shift Catalysts. *Science* **2003**, *301*, 935–938.
12. Bailie, J. E.; Hutchings, G. J. Promotion by Sulfur of Gold Catalysts for Crotyl Alcohol Formation from Crotonaldehyde Hydrogenation. *Chem. Commun.* **1999**, 2151–2152.
13. Biella, S.; Prati, L.; Rossi, M. Selective Oxidation of D-glucose on Gold Catalyst. *J. Catal.* **2002**, *206*, 242–247.
14. Herzing, A. A.; Kiely, C. J.; Carley, A. F.; Landon, P.; Hutchings, G. J. Identification of Active Gold Nanoclusters on Iron Oxide Supports for CO Oxidation. *Science* **2008**, *321*, 1331–1335.
15. Landon, P.; Collier, P. J.; Papworth, A. J.; Kiely, C. J.; Hutchings, G. J. Direct Synthesis of Hydrogen Peroxide from H_2/O_2 Using a Gold Catalyst. *Chem. Commun.* **2002**, 2058–2059.
16. Valden, M.; Lai, X.; Goodman, D. W. Onset of Catalytic Activity of Gold Clusters on Titania with the Appearance of Nonmetallic Properties. *Science* **1998**, *281*, 1647–1650.
17. Boyen, H.-G.; Kästle, G.; Weigl, F.; Koslowski, B.; Dietrich, C.; Ziemann, P.; Spatz, J. P.; Riethmüller, S.; Hartmann, C.; Möller, M.; *et al.* Oxidation-Resistant Gold-55 Clusters. *Science* **2002**, *297*, 1533–1536.
18. Mattthey, D.; Wang, J.G.; Matthiesen, W. J.; Schaub, R.; Lægsgaard, E.; Hammer, B; Besenbacher, F. Enhanced Bonding of Gold Nanoparticles on Oxidized TiO_2(110). *Science* **2007**, *315*, 1692–1696.
19. Yoon, B.; Häkkinen, H.; Landman, U.; Wörz, A. S.; Antonietti, J.-M.; Abbet, S.; Judai, K.; Heiz, U. Charging Effects on Bonding and Catalyzed Oxidation of CO on Au_8 Clusters on MgO. *Science* **2005**, *307*, 403–407.
20. Gao, Y.; Shao, N.; Bulusu, S.; Zeng, X.C. Effective CO Oxidation on Endohedral Gold-Cage Nanoclusters. *J. Phys. Chem. C* **2008**, *112*, 8234–8238.
21. Chen, M. S.; Cai, Y.; Yan, Z.; Goodman, D. W. On the Origin of the Unique Properties of Supported Au Nanoparticles. *J. Am. Chem. Soc.* **2006**, *128*, 6341–6346.
22. Minato, T.; Susaki, T.; Shiraki, S.; Kato, H. S.; Kawai, M.; Aike, K. Investigation of the Electronic Interaction between TiO_2(110) Surface and Au Clusters by PES and STM. *Surf. Sci.* **2004**, *566*, 1012–1017.
23. Diemant, T.; Zhao, Z.; Rauscher, H.; Bansmann, J.; Behm, R. J. Interaction of CO with Planar Au/TiO_2 Model Catalysts at Evaluated Pressures. *Tops. Catal.* **2007**, *44*, 83–89.
24. Rodriguez, J.A.; Wang, X.; Liu, P.; Wen, W.; Hanson, J. C.; Hrbek, J.; Pérez, M.; Evans, J. Gold Nanoparticles on Ceria: Importance of O Vacancies in the Activation of Gold. *Tops. Catal.* **2007**, *44*, 73–81.
25. Gong, J.; Ojifinni, R. A.; Kim, T. S.; Stiehl, J. D.; McClure, S. M.; White, J. M.; Mullins, C. B. Low Temperature CO Oxidation on Au(111) and the Role of Adsorbed Water. *Tops. Catal.* **2007**, *44*, 57–63.
26. Janssens, T. V. W.; Clausen, B. S.; Hvolbæk, B.; Falsig, H.; Christensen, C. H.; Bligaard, T.; Nøskov, J. K. Insights into the Reactivity of Supported Au Nanoparticles: Combining Theory and Experiments. *Tops. Catal.* **2007**, *44*, 15–26.
27. Wang, J. G.; Hammer, B. Some Recent Theoretical Advances in the Understanding of the Catalytic Activity of Au. *Tops. Catal.* **2007**, *44*, 49–56.
28. Roldán, A.; González, S.; Ricart, J.M.; Illas, F. Critical Size for O_2 Dissociation by Au Nanoparticles. *ChemPhysChem* **2009**, *10*, 348–351.
29. Salisbury, B. E.; Wallace, W. T.; Whetten, R. L. Low-Temperature Activation of Molecular Oxygen by Gold Clusters: A Stoichiometric Process Correlated to Electron Affinity. *Chem. Phys.* **2000**, *262*, 131–141.
30. Stolcic, D.; Fisher, M.; Ganteför, G.; Kim, Y. D.; Sun, Q.; Jena, P. Direct Observation of Key Reaction Intermediates on Gold Clusters. *J. Am. Chem. Soc.* **2003**, *125*, 2848–2849.

31. Lopez, N.; Nøskov, J. K. Catalytic CO Oxidation by a Gold Nanoparticle: A Density Functional Study. *J. Am. Chem. Soc.* **2002**, *124*, 11262–11263.

32. Cox, D. M.; Brickman, R.; Creegan, K; Kaldor, A. Z. Gold Clusters: Reactions and Deuterium Uptake. *Z. Phys. D.* **1991**, *19*, 353–355.

33. Cox, D. M.; Brickman, R.; Creegan, K. Studies of the Chemical Properties of Size Selected Metal Clusters: Kinetics and Saturation. *Mater. Res. Soc. Symp. Proc.* **1991**, *206*, 34–48.

34. Hernández, N. C.; Sanz, J. F.; Rodriguez, J. A. Unravelling the Origin of the High-Catalytic Activity of Supported Au: A Density-Functional Theory-Based Interpretation. *J. Am. Chem. Soc.* **2006**, *128*, 15600–15601.

35. Rashkeev, S. N.; Lupini, A. R.; Overbury, S. H.; Pennycook, S. J.; Pantelides, S. T. Role of the Nanoscale in Catalytic CO Oxidation by Supported Au and Pt Nanostructures. *Phys. Rev. B* **2007**, *76*, 035438-1−035438-8.

36. Guzman, J.; Gates, B. C. Catalysis by Supported Gold: Correlation between Catalytic Activity for CO Oxidation and Oxidation States of Gold. *J. Am. Chem. Soc.* **2004**, *126*, 2672–2673.

37. Gao, W.; Chen, X. F.; Li, J. L.; Jiang, Q. Is Au_{55} or Au_{38} Cluster a Threshold Catalyst for Styrene Epoxidation? *J. Phys. Chem. C* **2010**, *114*, 1148–1153.

38. Cuzman, J.; Carrettin, S.; Corma, A. Spectroscopic Evidence for the Supply of Reactive Oxygen during CO Oxidation Catalyzed by Gold Supported on Nanocrystalline CeO_2. *J. Am. Chem. Soc.* **2005**, *127*, 3286–3287.

39. Sinha, A. K.; Seelan, S.; Tsubota, S.; Haruta, M. A Three-Dimensional Mesoporous Titanosilicate Support for Gold Nanoparticles: Vapor-Phase Epoxidation of Propene with High Conversion. *Angew. Chem. Int. Ed.* **2004**, *43*, 1546–1548.

40. See a recent review on Au_{55} cluster and references therein: Schmid, G. The Relevance of Shape and Size of Au_{55} Clusters. *Chem. Soc. Rev.* **2008**, *37*, 1909–1930.

41. Jadzinsky, P. D.; Calero, G.; Ackerson, C. J.; Bushnell, D. A.; Kornberg1, R. D. Structure of a Thiol Monolayer-Protected Gold Nanoparticle at 1.1 Å Resolution. *Science* **2007**, *318*, 430–433.

42. Gao, Y.; Shao, N.; Zeng, X. C. Ab Initio Study of Thiolate-Protected Au_{102} Nanocluster. *ACS Nano* **2008**, *2*, 1497–1503.

43. Heaven, M. W.; Dass, A.; White, P. S.; Holt, K. M.; Murray, R. W. Crystal Structure of the Gold Nanoparticle $[N(C_8H_{17})_4][Au_{25}(SCH_2CH_2Ph)_{18}]$. *J. Am. Chem. Soc.* **2008**, *130*, 3754–3755.

44. Akola, J.; Walter, M.; Whetten, R. L.; Hakkinen, H.; Gronbeck, H. On the Structure of Thiolate-Protected Au_{25}. *J. Am. Chem. Soc.* **2008**, *130*, 3756–3757.

45. Zhu, M.; Aikens, C. M.; Hollander, F. J.; Schatz, G. C.; Jin, R. Correlating the Crystal Structure of A Thiol-Protected Au_{25} Cluster and Optical Properties. *J. Am. Chem. Soc.* **2008**, *130*, 5883–5885.

46. Tsunoyama, H.; Nickut, P.; Negishi, Y.; Al-Shamery, K.; Matsumoto, Y.; Tsukuda, T. Formation of Alkanethiolate-Protected Gold Clusters with Unprecedented Core Sizes in the Thiolation of Polymer-Stabilized Gold Clusters. *J. Phys. Chem. C* **2007**, *111*, 4153–4158.

47. Pei, Y.; Gao, Y.; Zeng, X. C. Structural Prediction of Thiolate-Protected Au_{38}: A Face-Fused Bi-icosahedral Au Core. *J. Am. Chem. Soc.* **2008**, *130*, 7830–7832.

48. Lopez-Acevedo, O.; Akola, J.; Whetten, R. L.; Grönbeck, H.; Häkkinen, H. Structure and Bonding in the Ubiquitous Icosahedral Metallic Gold Cluster $Au_{144}(SR)_{60}$. *J. Phys. Chem. C* **2009**, *113*, 5035–5038.

49. Dass, A. Mass Spectrometric Identification of $Au_{68}(SR)_{34}$ Molecular Gold Nanoclusters with 34-Electron Shell Closing. *J. Am. Chem. Soc.* **2009**, *131*, 11666–11667.

50. Jiang, D.; Tiago, M. L.; Luo, W.; Dai, S. The "Staple" Motif: A Key to Stability of Thiolate-Protected Gold Nanoclusters. *J. Am. Chem. Soc* **2008**, *130*, 2777–2779.

51. Pei, Y.; Gao, Y.; Shao, N.; Zeng, X. C. Thiolate-Protected $Au_{20}(SR)_{16}$ Cluster: Prolate Au_8 Core with New $[Au_3(SR)_4]$ Staple Motif. *J. Am. Chem. Soc.* **2009**, *131*, 13619–13621.

52. Tsunoyama, H.; Ichikuni, N.; Sakurai, H.; Tsukuda, T. Effect of Electronic Structures of Au Clusters Stabilized by Poly(*N*-vinyl-2-pyrrolidone) on Aerobic Oxidation Catalysis. *J. Am. Chem. Soc.* **2009**, *131*, 7086–7093.

53. Zhu, Y.; Qian, H.; Drake, B. A.; Jin, R. Atomically Precise $Au_{25}(SR)_{18}$ Nanoparticles as Catalysts for the Selective Hydrogenation of α. *Angew. Chem., Int. Ed.* **2010**, *49*, 1295–1298.

54. Fairbanks, M. C.; Benfield, R. E.; Newport, R. J.; Schmid, G. An EXAFS Study of the Cluster Molecule $Au_{55}(PPh_3)_{12}Cl_6$. *Solid State Commun.* **1990**, *73*, 431–436.

55. Benfield, R. E.; Grandjean, D.; Kroll, M.; Pugin, R.; Sawitowski, T.; Schmid, G. Structure and Bonding of Gold Metal Clusters, Colloids, and Nanowires Studied by EXAFS, XANES, and WAXS. *J. Phys. Chem. B* **2001**, *105*, 1961–1970.

56. Vogel, W.; Rosner, B.; Tesche, B. Organometallic Complexes by X-ray Power Diffraction and Transmission Electron Microscopy. *J. Phys. Chem.* **1993**, *97*, 11611–11616.

57. Rapoport, D. H.; Vogel, W.; Cölfen, H.; Schlögl, R. Ligand-Stabilized Metal Clusters: Reinvestigation of the Structure of $Au_{55}[P(C_6H_5)_3]_{12}Cl_6$. *J. Phys. Chem. B* **1997**, *101*, 4175–4183.

58. Wales, D. J.; Scheraga, H. A. Global Optimization of Clusters, Crystals, and Biomolecules. *Science* **1999**, *285*, 1368–1372.

59. Yoo, S.; Zeng, X. C. Motif Transition in Growth Pattern of Small-to-Medium Sized Silicon Clusters. *Angew. Chem., Int. Ed.* **2005**, *44*, 1491–1494.

60. Huang, W.; Ji, M.; Dong, C.-D.; Gu, X.; Wang, L.-M.; Gong, X. G.; Wang, L.-S. Relativistic Effects and the Unique Low-Symmetry Structures of Gold Nanoclusters. *ACS Nano* **2008**, *2*, 897–904.

61. Briant, C. E.; Theobald, R.C.; White, J. W.; Bell, L. K.; Mingos, D. M. P. Synthesis and X-Ray Structural Characterization of the Centred Icosahedral Gold Cluster Compound $[Au_{l3}(PMe_2Ph)_{10}C1_2](PF_6)_3$: The Realization of a Theoretical Prediction. *J. Chem. Soc., Chem. Commun.* **1981**, 201–206.

62. Teo, B. K.; Shi, X.; Zhang, H. Pure Gold Cluster of 1:9:9:1:9:9: 1 Layered Structure: A Novel 39-Metal-Atom Cluster $[(Ph_3P)_{14}Au_{39}Cl_6]Cl_2$ with an Interstitial Gold Atom in a Hexagonal Antiprismatic Cage. *J. Am. Chem. Soc.* **1992**, *114*, 2743–2744.

63. Periyasamy, G.; Remacle, F. Ligand and Solvation Effects on the Electronic Properties of Au_{55} Clusters: A Density Functional Theory Study. *Nano Lett.* **2009**, *9*, 3007–3011.

64. Liu, Z-P.; Hu, P.; Alavi, A. Catalytic Role of Gold in Gold-Based Catalysts: A Density-Functional Theory Study on the CO Oxidation on Gold. *J. Am. Chem. Soc.* **2002**, *124*, 14770–14779.

65. Okumura, M.; Kitagawa, Y.; Kawakami, T.; Haruta, M. Theoretical Investigation of the Heterojunction Effect in PVP-stabilized Au_{13} Clusters. The Role of PVP in their Catalytic Activities. *Chem. Phys. Lett.* **2008**, *459*, 133–136.

66. Sanchez, A.; Abbet, S.; Heiz, U.; Schneider, W. D.; Hakkinen, H.; Barnett, R. N.; Landman, U. When Gold IS Not Noble: Nanoscale Gold Catalysts. *J. Phys. Chem. A* **1999**, *103*, 9573–9578.

67. An, W.; Pei, Y.; Zeng, X. C. CO Oxidation Catalyzed by Single-Walled Helical Gold Nanotube. *Nano Lett.* **2008**, *8*, 195–202.

68. Gao, Y.; Shao, N.; Pei, Y.; Zeng, X. C. Crown Gold $Cu_{13}@Au_{42}$ Core-Shell Nanoparticle with High Catalytic Activity. *Nano Lett.* **2010**, *10*, 1055–1062.

69. Torres, D.; Illas, F. On the Performance of Au(111) for Ethylene Epoxidation: A Density Functional Study. *J. Phys. Chem. B* **2006**, *110*, 13310–11313.

70. Deng, X.; Friend, C. M. Selective Oxidation of Styrene on an Oxygen-Covered Au(111). *J. Am. Chem. Soc.* **2005**, *127*, 17178.

71. Enever, M.; Linic, S.; Uffalussy, K.; Vohs, J. M.; Barteau, M. A.

ARTICLE

Synthesis, Structure, and Reactions of Stable
Oxametallacycles from Styrene Oxide on Ag(111). *J. Phys. Chem. B* **2005**, *109*, 2227–2233.

72. Delley, B. An All-Electron Numerical Method for Solving the Local Density Functional for Polyatomic Molecules. *J. Chem. Phys.* **1990**, *92*, 508–517 (DMol^3 is available from Accelrys in version 4.3).

73. Perdew, J. P.; Burke, K.; Ernzerhof, M. Generalized Gradient Approximation Made Simple. *Phys. Rev. Lett.* **1996**, *77*, 3865–3868.

74. Bürgel, C.; Reilly, N. M.; Johnson, G. E.; Mitrić, R.; Kimble, M. L.; Castleman, A. W., Jr.; Bonačić-Koutechk, V. Influence of Charge State on the Mechanism of CO Oxidation on Gold Clusters. *J. Am. Chem. Soc.* **2008**, *130*, 1694–1698.

75. Liu, R.; Ke, S-H; Baranger, H. U.; Yang, W. Negative Differential Resistance and Hysteresis Through an Organometallic Molecule from Molecular-Level Crossing. *J. Am. Chem. Soc.* **2006**, *128*, 6274–6275.

76. Wang, C-M; Fan, K-N; Liu, Z-P. Origin of Oxide Selectivity in Gold-Based Catalysts: A First Principle Study of CO Oxidation Over Au Supported on Monoclinic and Tetragonal ZrO$_2$. *J. Am. Chem. Soc.* **2007**, *129*, 2642–2647.

77. Dolg, M.; Wedig, U.; Stoll, H.; Preuss, H. Energy-Adjusted *ab Initio* Pseudopotentials for the First Row Transition Elements. *J. Chem. Phys.* **1987**, *86*, 866–872.

78. Bergner, A.; Dolg, M.; Küchle, W.; Stoll, H.; Preuss, H. *Ab Initio* Energy-Adjusted Pseudopotentials for Elements of Groups 13−17. *Mol. Phys.* **1993**, *80*, 1431–1441.